# An Improved Template-Matching-Based Pose Tracking Method for Planar Nanopositioning Stages Using Enhanced Correlation Coefficient

Hai Li, Xianmin Zhang, Sheng Yao, Benliang Zhu, and Sergej Fatikow

***Abstract*—In the development and application of planar nanopositioning stages (PNSs), there is an urgent need to measure pose quickly and accurately. An improved pose measurement method based on template matching that can track in-plane three degree-of-freedom (3-DOF) motion at small scale with high performance is presented in this paper. To achieve higher tracking accuracy and robustness, the problem of pose measurement is first transformed into an enhanced correlation coefficient (ECC) -based parametric image matching problem. Subsequently, an efficient 3-DOF tacking algorithm based on inverse compositional searching strategy is developed in which the update of Hessian matrix caused by the nonlinear warp is avoided to improve the tracking frame rate. A series of simulations and experiments are conducted to evaluate the performance of the proposed method. The results show that the use of ECC can effectively improve the tracking robustness and accuracy, especially for angular measurement, compared to the sum of square difference (SSD) criterion. Besides, the tracking frame rate can be improved by using the developed algorithm even though the correlation function is much more complicated. Finally, application of the proposed method on a nanorobotic system for automatic in-plane 3-DOF alignment is demonstrated.**

***Index Terms*— Nanopositioning stages, pose tracking, enhanced correlation coefficient, template matching.**
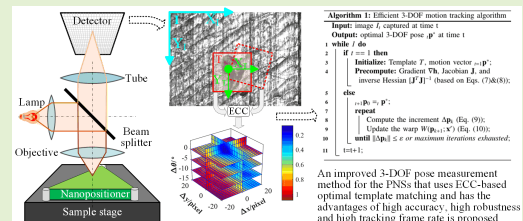
I. INTRODUCTION

DUE to the large demand for planar nanopositioning stages (PNSs) in many practical applications, e.g., wafer-level integrated circuit inspection, ultra-precision machining, and

Hai Li and Sergej Fatikow are with the Guangdong Key Laboratory of Precision Equipment and Manufacturing Technology, School of Mechanical and Automotive Engineering, South China University of Technology, Guangzhou 510641, China, and also with the Division of Microrobotics and Control Engineering, Department of Computing Science, University of Oldenburg, 26129 Oldenburg, Germany (e-mail: lihai@scut.edu.cn; sergej.fatikow@uni-oldenburg.de).

Xianmin Zhang, Sheng Yao, and Benliang Zhu are with the Guangdong Key Laboratory of Precision Equipment and Manufacturing Technology, School of Mechanical and Automotive Engineering, South China University of Technology, Guangzhou 510641, China (e-mail: zhangxm@scut.edu.cn; me_syao@mail.scut.edu.cn; meblzhu@scut.edu.cn).

nanomanipulation of small objects [1]–[4], it has recently drawn a lot of attentions [5]–[9]. Among all the factors (e.g., mechanical design, actuation, sensing, and control) that affect performance of the PNS, sensing technique is now one of the most important factors restricting development and application of the PNSs [10]–[13].

The reason for the difficulty in measurement lies in the coupling of the 3-DOF pose, in particular the coupling between the rotational component (θ) and the translational components (x,y). Although many kinds of sensors with nanometer or micro-radian resolution, such as capacitive displacement sensor (CDS), laser displacement sensor (LDS) and optic encoders, can be found in the market, most of them are single-DOF sensors and cannot be directly used to measure coupled 3-DOF motion. To solve this problem, a common solution widely used in the community of precision positioning is to use three linear displacement sensors (e.g., LDS and CDS) for combined measurement [6], [12]. In this scheme, the three sensors are distributed around the moving part of the PNS with known locations and the rotation angle is measured by utilizing the anti-trigonometric function. In addition to the multi-sensor-based method, another technique that has been reported for multi-DOF motion measurement is laser interferometry [14], [15]. For instance, by integrating

the interferometry with an extra counter-rotation stage system (for rotation compensation), dynamically measurement of the 3-DOF pose with high precision is realized [14]. By using one reference retroreflector and an assembled measurement mirror composed of two corner cubes, Zhao *et al.* [15] realized multi-DOF measurement based on heterodyne interferometer. Although the above-mentioned methods can effectively measure planar 3-DOF motion, the price is additional components (e.g., sensors, lenses or mechanical stages) and increased structural complexity. Moreover, the measurement range of the rotation angle of these methods is normally limited to several millimeter-radian.

Recently, vision-based multi-DOF motion measurement at small scale has been attracting much attention because of its non-contact, low-cost, and high flexibility [16]–[26]. Based on the used principles, these methods can be roughly cataloged into the feature-based methods [17], [18], the template-matching-based methods (TMBMs) [19]–[23], the phase-correlation-based methods [24], [25], and other methods that combines multi-image processing techniques [26]. Among these methods, TMBM is the simplest and most widely used method in planar motion tracking because of its high robustness, high precision, and needless for tracking-markers [19]–[23]. For instances, by utilizing the coarse-to-fine searching strategy, Zhang *et al.* [19] and Zhao *et al.* [20] realized precise 2-DOF displacement measurement with the accuracy at nanoscale. In Ref. [21], a three-step matching method that is robust to illumination is proposed for LED chip positioning. However, the basic principle of conventional TMBMs (e.g., slide the template over the entire image to find the best matching location) has caused two drawbacks (only suitable for translation movement and heavy computational cost) that limit its use for planar 3-DOF motion tracking [23].

In the community of digital image correlation (DIC), TMBMs have been widely used for full-field deformation measurement for long time [27]. To overcome the disadvantage of heavy computational cost, many efforts including optimal searching based on numerical optimization [28], [29] and parallel computing [30] are developed. According to the review works shown in Refs. [27], [30], one can find that for personal-computer-based applications, the best and easiest way to increase matching speed is using optimization techniques. In addition to improving computational speed, research works related to increasing measurement flexibility, accuracy, and robustness have also been proposed. For instances, Refs. [31] and [32] are robust to large rotations and can be used to measure the rotation angle in the full-field measurement applications. In Ref. [33], a path-independent digital image correlation method that is robust for deformation discontinuity has been demonstrated. Although the above references from the DIC community are instructive for our research, the problem faced in this article is different from them, as our measurement goal is to continuously measure planar 3-DOF rigid motion in realtime (not full-field deformation at one moment). Besides, compared to the linear affine warp used in DIC, the warp function in our problem is nonlinear since the rotation component is involved, thus making the optimization more complicated. In Ref. [34], an effective 3-DOF motion tracking method based on TM is proposed. The results demonstrate that it can realize online 3-DOF motion tracking with acceptable accuracy. Nevertheless, since the correlation function used in Ref. [34] is the sum of squared difference (SSD), the tracking performance can be easily disturbed when there are image noise and luminosity distortions. Moreover, due to the re-calculation of Hessian in tracking loops, the achieved tracking frame rate is limited to 30 Hz.

In this paper, a template-matching-based 3-DOF motion tracking method that can realize is presented. To improve tracking robustness and accuracy, a much more complex but more robust correlation criterion, the enhanced correlation coefficient (ECC), is introduced for planar 3-DOF motion tracking, which allows for uneven illumination and image noise. Moreover, an algorithm based on inverse compositional Gauss-newton (ICGN) is developed to realize 3-DOF motion tracking with subpixel accuracy and high frame rate. A series of simulations and experiments are implemented to evaluate performance of the proposed method. Finally, the proposed pose tracking method is applied to a robotic-based micro-manipulation system for automated in-plane 3-DOF alignment.

The remainder of this paper is organized as follows. Section II gives the basic principle for planar 3-DOF motion trakcing. Section III presents the improved tracking algorithm, including the ECC criterion and iterative optimization scheme. The effectiveness and performance of the proposed method are tested in Section IV. The application of the proposed method for automated alignment of a probe and a substrate is demonstrated in Section V. Finally, conclusions are given in Section VI.

II. PROBLEM FORMULATION: PLANAR 3-DOF TEMPLATE MATCHING

In order to measure pose of the PNS using vision technique, a stationary vision system that can obtain enlarged image of the partial surface of the PNS is indispensable. Fig. 1(a) shows the configuration of a typical optical microscopy vision system with reflected lighting. Fig. 1 (b) shows the simplified geometric model of the microscope vision system in which f, d, M represent focal length, working distance, and magnification ratio, respectively.

As illustrated in Fig. 1 (c), suppose $I_0(x, y)$ is the image obtained by the vision system at $t = 0$ and T be the template extracted from I_0. Apparently, as the nanopositioner moves, the gray-value corresponding to each pixel of the image will change while the distribution characteristics of the image will remain consistent. Let $O_I - xy$ be the stationary frame of the image with its homogeneous pixel coordinates of $\mathbf{x} = (x, y, 1)$, $O_T - x'y'$ be the moving frame attached to the template with the homogeneous pixel coordinates of $\mathbf{x}' = (x', y', 1)$, and Ω be the set of all the pixels' coordinates in T, the problem of 3-DOF template matching can then be expressed as

$$\mathbf{p} = \underset{\mathbf{p}}{min/max} \sum_{\mathbf{x}' \in \Omega} \mathcal{R}(I(W(\mathbf{p}; \mathbf{x}')), T(\mathbf{x}')) \qquad (1)$$

where $\mathcal{R}$ is a kind of matching criterion (Fig. 1(d) demonstrates the ECC matching distribution near the real-solution)
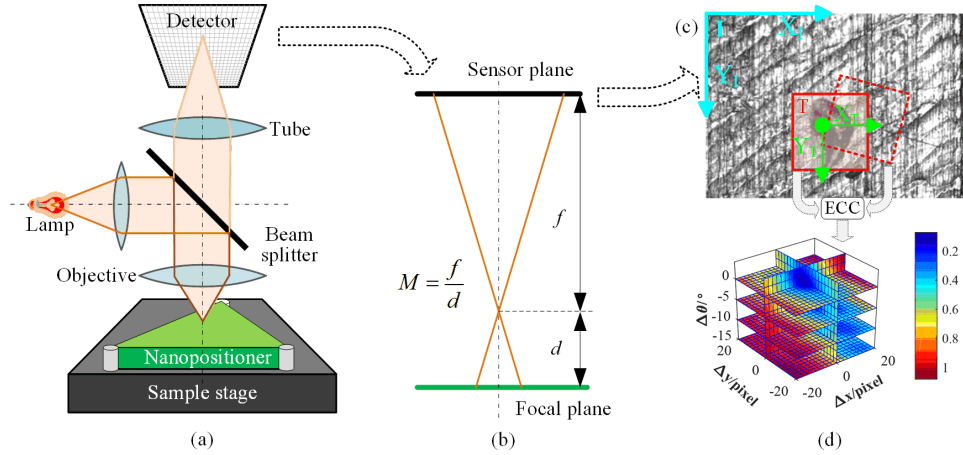
Fig. 1. The ECC-based template matching method for 3-DOF pose tracking; (a) the simplified schematic diagram of the vision system; (b) the simplified geometric model of the vision system; (c) the coordinate systems for planar 3-DOF template matching ($O_I - xy$ and $O_T - xy$); (d) the ECC matching results obtained by calculating the correlation between the original template and the adjacent sub-image area (surrounded by the dash line in (c)).

and $\mathbf{p} = (t_x, t_y, \theta)^T$ is the parameter vector that defines the transformation warp W between the frames $O_T - x'y'$ and $O_I - xy$. For the planar Euclidean transform, the warp W can be written as

$$\mathbf{x} = \begin{bmatrix} cos(\theta) & sin(\theta) & t_x \\ -sin(\theta) & cos(\theta) & t_y \\ 0 & 0 & 1 \end{bmatrix} \mathbf{x}' = \begin{bmatrix} W_x \\ W_y \\ 1 \end{bmatrix} = W(\mathbf{p}; \mathbf{x}') \quad (2)$$

Note that by solving Eq. (1), 3-DOF pose of the nanopositioner expressed in image space can be obtained. To acquire pose results in physical space, a transformation based on the geometric model of the vision system is needed. Ignoring the lens distortion, the conversion can be expressed as

$$\mathbf{p}_{phy} = \begin{bmatrix} f_x & 0 & 0 \\ 0 & f_y & 0 \\ 0 & 0 & 1 \end{bmatrix} \mathbf{p} \quad (3)$$

where f_x and f_y are the intrinsic parameters of the vision system [35].

III. 3-DOF POSE TRACKING BASED ON ENHANCED CORRELATION COEFFICIENT (ECC)

A. The ECC Matching Criterion

The ECC was proposed by Evangelidis and Psarakis in 2008 [36] for robust parametric image alignment in stereo matching. Let $\mathbf{h}(\mathbf{x}') = [T(\mathbf{x}'_1), T(\mathbf{x}'_2), \cdots, T(\mathbf{x}'_N)]^T$ be the vector of all the pixels' gray value, N be the total number of pixels in the template and $\mathbf{g}(\mathbf{x}') = [I(W(\mathbf{p}; \mathbf{x}'_1)), I((W\mathbf{p}; \mathbf{x}'_2)), \cdots, I(W(\mathbf{p}; \mathbf{x}'_N))]^T$ be the corresponding vector of the sub-image, the ECC can be expressed as

$$\mathcal{R}_{ECC}(\mathbf{p}) = \left\| \frac{\mathbf{h}(\mathbf{x}') - \bar{h}}{\Delta h} - \frac{\mathbf{g}(W(\mathbf{p}; \mathbf{x}')) - \bar{g}}{\Delta g} \right\|^2 \quad (4)$$

where $\| \cdot \|$ denotes the Euclidean norm, $\bar{h} = \frac{1}{N} \sum_{n=1}^{N} T(\mathbf{x}'_i)$, $\bar{g} = \frac{1}{N} \sum_{n=1}^{N} I(W(\mathbf{p}; \mathbf{x}'_i))$, $\Delta h = \|\mathbf{h}(\mathbf{x}') - \bar{h}\|$, and $\Delta g = \|\mathbf{g}(W(\mathbf{p}; \mathbf{x}')) - \bar{g}\|$.

B. Optimization of the ECC Based on the Inverse Compositional Gauss-Newton Method

In Ref. [36], to effectively solve the ECC-based matching problem, the ECC criterion is first switched to a cross cor-relation form and then a linear approximation is made and its closed-form solution (per iteration) is obtained based on classified discussion. Although a good convergent accuracy can be obtained, the steps for solving the closed-form solution is complicated and the computational cost is thus very heavy. Besides, the nonlinear warp function used in this paper also causes difficulty to the optimization. To simplify the solving process, an optimization algorithm which combines the inverse compositional scheme and Gauss-Newton method is developed.

To optimize the ECC criterion using inverse compositional scheme [28], [37], the objective function at k^{th} iteration can be expressed as

$$\mathcal{R}_{ECC}(\Delta \mathbf{p}_k) = \left\| \frac{\mathbf{h}(W(\Delta \mathbf{p}_k; \mathbf{x}')) - \bar{h}}{\Delta h} - \frac{\mathbf{g}(W(\mathbf{p}_k; \mathbf{x}')) - \bar{g}}{\Delta g} \right\|^2 \quad (5)$$

where $\bar{h}$ and Δh are two constant values since they are only related to the gray value of the template. To obtain the increment $\Delta \mathbf{p}_k$, one can first perform a first-order Tylor expansion of Eq. (5) with respect to $\Delta \mathbf{p}_k$, which yields

$$\mathcal{R}_{ECC}(\Delta \mathbf{p}_k) = \left\| \frac{\mathbf{h}(\mathbf{x}') + \mathbf{J} \Delta \mathbf{p}_k - \bar{h}}{\Delta h} - \frac{\mathbf{g}(W(\mathbf{p}_k; \mathbf{x}')) - \bar{g}}{\Delta g} \right\|^2 \quad (6)$$

where $\mathbf{J}$ denotes the Jacobian matrix, and its expression can be written as

$$\mathbf{J}_{N \times 3} = [\nabla \mathbf{h}_x, \nabla \mathbf{h}_y]_{N \times 2} \begin{bmatrix} \frac{\partial W_x}{\partial \mathbf{p}} \\ \frac{\partial W_y}{\partial \mathbf{p}} \end{bmatrix}_{2 \times 3} = \nabla \mathbf{h} \frac{\partial W}{\partial \mathbf{p}} \quad (7)$$

where $\nabla \mathbf{h}_x$ and $\nabla \mathbf{h}_y$ are the gradients of the template ordered in vectors, $\frac{\partial W_x}{\partial \mathbf{p}}$ and $\frac{\partial W_y}{\partial \mathbf{p}}$ are the Jacobian matrix of the warp

function W with respect to $\mathbf{p}$. Based on the warp function shown in Eq. (2), one can obtain

$$\begin{bmatrix} \dfrac{\partial W_x}{\partial \mathbf{p}} \\ \dfrac{\partial W_y}{\partial \mathbf{p}} \end{bmatrix} = \begin{bmatrix} -sin(\theta)x' + cos(\theta)y' & 1 & 0 \\ -cos(\theta)x' - sin(\theta)y' & 0 & 1 \end{bmatrix} \quad (8)$$

By solving $\frac{\partial \mathcal{R}(\Delta \mathbf{p}_k)}{\partial \Delta \mathbf{p}_k} = 0$, the $\Delta \mathbf{p}_k$ with respect to the extreme of Eq. (6) can be solved as

$$\Delta \mathbf{p}_k = -[\mathbf{J}^T \mathbf{J}]^{-1} \mathbf{J}^T \left[(\mathbf{h}(\mathbf{x}') - \bar{h}) - \frac{\Delta h}{\Delta g} (\mathbf{g}(W(\mathbf{p}_k; \mathbf{x}')) - \bar{g}) \right] \quad (9)$$

where $[\mathbf{J}^T \mathbf{J}]^{-1}$ is called the Hessian matrix. After obtaining $\Delta \mathbf{p}_k = (\Delta \theta_k, \Delta t_{xk}, \Delta t_{yk})^T$, the warp function is updated by

$$W(\mathbf{p}_{k+1}; \mathbf{x}') \leftarrow W(\mathbf{p}_k; \mathbf{x}') \circ W^{-1}(\Delta \mathbf{p}_k; \mathbf{x}')$$
$$= \begin{bmatrix} cos\theta_k & sin\theta_k & t_{xk} \\ -sin\theta_k & cos\theta_k & t_{yk} \\ 0 & 0 & 1 \end{bmatrix} \begin{bmatrix} cos\Delta\theta_k & sin\Delta\theta_k & \Delta t_{xk} \\ -sin\Delta\theta_k & cos\Delta\theta_k & \Delta t_{yk} \\ 0 & 0 & 1 \end{bmatrix}^{-1} \mathbf{x}' \quad (10)$$

where $W^{-1}(\Delta \mathbf{p}_k; \mathbf{x}')$ is the inverse increment warp matrix and "$\circ$" represents the step of warp compositional.

C. Efficient 3-DOF Motion Tracking Without the Re-Calculation of the Hessian Matrix

Once the optimization scheme is determined, an efficient 3-DOF motion tracking algorithm which mainly contains two loops is developed, as shown in **Algorithm 1**. The outer loop is mainly responsible for acquiring image frame and setting initial guess for the ICGN approach, and the inner loop is the main loop of the ICGN approach. When $t = 1$, the outer loop is also responsible for selecting the template from the first captured image and then performing the pre-calculation of $\nabla \mathbf{h}$, $\mathbf{J}$, and $[\mathbf{J}^T \mathbf{J}]^{-1}$.

Note that, according to Eqs. (7) and (8), the Jacobian matrix $\mathbf{J}$ and inverse Hessian $[\mathbf{J}^T \mathbf{J}]^{-1}$ are related to the warp parameter θ and thus are non-constant when θ changes. For the ICGN approach, it is easy to understand that for inner iterations at a certain outer loop, there is no need to recalculate the Hessian and Jacobian because the increment $\Delta \mathbf{p}_k$ is always expanded with respect to the initial guess of $\mathbf{p}$. However, the Jacobian and Hessian need to be updated when a new outer loop starts (θ has changed), theoretically. Nevertheless, we found that when the motion between two consecutive image sequences is relatively small, the ICGN algorithm can still converge with high accuracy and speed even without updating the Hessian matrix. This is reasonable because for GN optimization with small residual errors, the necessary and sufficient condition for convergence is that the Hessian matrix is positive definite [38]. In actual tracking, since the gray values inside a template are very rich, the positive definiteness of the template's Hessian matrix can be easily guaranteed.

Algorithm 1 Efficient 3-DOF Motion Tracking Algorithm

Input: image I_t captured at time t
Output: optimal 3-DOF pose $_t\mathbf{p}^*$ at time t
1 **while** *1* **do**
2   **if** $t == 1$ **then**
3   **Initialize:** Template T, motion vector $_{t=1}\mathbf{p}^*$;
4   **Precompute:** Gradient $\nabla\mathbf{h}$, Jacobian $\mathbf{J}$, and inverse Hessian $[\mathbf{J}^T\mathbf{J}]^{-1}$ (based on Eqs. (7)&(8));
5   **else**
6      $_{t+1}\mathbf{p}_0 =_t \mathbf{p}^*$;
7   **repeat**
8   Compute the increment $\Delta\mathbf{p}_k$ (Eq. (9));
9   Update the warp $W(\mathbf{p}_{k+1}; \mathbf{x}')$ (Eq. (10));
10   **until** $\|\Delta\mathbf{p}_k\| \leq \varepsilon$ *or maximum iterations exhausted*;
11   t=t+1;

IV. PERFORMANCE EVALUATION OF THE 3-DOF POSE TRACKING METHOD

In order to effectively evaluate the performance of the proposed 3-DOF pose tracking method, a series of simulations and experiments are conducted. Note that in the simulations, image sequences with exactly know motion are utilized, hence the results can be used to estimate theoretic performance (in image space) of the proposed method. In the experiments, the tracking algorithm is implemented for pose tracking of a practical PNS and the measurement results (in physical measurement space) are compared to the classic 3-CDS based 3-DOF pose measurement scheme.

A. Simulation Tests

1) Simulation Scheme for Generating Image Sequence With Known Motions: The steps for preparing an image video containing a certain number of frames with know 3-DOF motions are designed as follows. Firstly, an original microscopic image obtained with uneven illumination is chosen (Fig. 2(a)) and its reflected component (Fig. 2(b)) and incident component (Fig. 2(c)) are obtained by using the Retinex image enhancement method [39], [40]. Secondly, the 3-DOF motions $\mathbf{p} = (x, y, \theta)^T = [p_1, p_2, p_3]^T$ used in the simulation are defined as

$$p_{i,j} = A_i cos(\tfrac{2\pi}{NoP}j) \quad i = 1, 2, 3; \quad j = 1, 2, \cdots, Nop \quad (11)$$

where A_i denotes the amplitude of the ith component of $\mathbf{p}$ and Nop represents the number of the sampled points in a cycle. Figs. 2(d) and (e) show examples of the 3-DOF motions in three-dimension trajectory and separate components with $A_1 = A_2 = 100 \ pixel$, $A_3 = 20 \ degree$ and $Nop = 160$, respectively. Thirdly, geometric transformations corresponding to each of the discrete motions and other needed manipulations (e.g., image noise and uneven illumination) are performed on the reflected image to generate the image sequences. Finally, these images are cropped to have the standard resolution of 640×480.

To evaluate the performance of the proposed method, three group of simulations are performed. In the first two
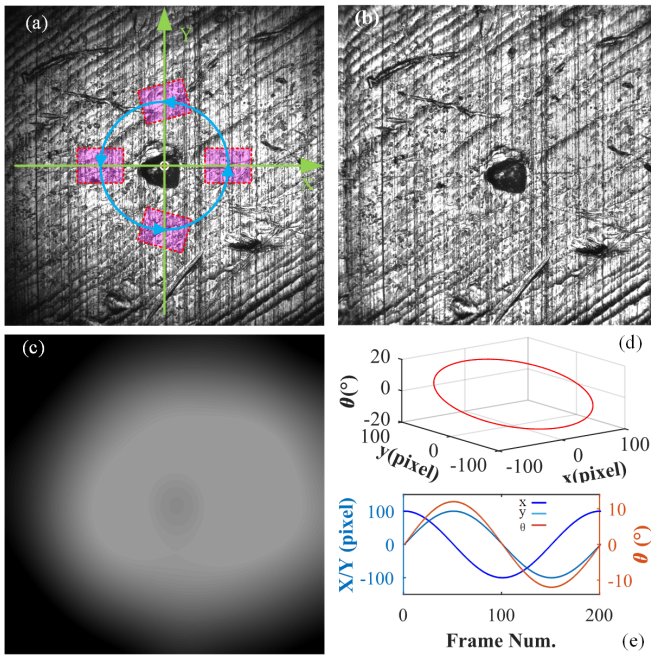
Fig. 2.   The scheme for generating image sequences with known motions. (a) the original microscopic image with uneven illumination; (b) and (c) the reflected component and incident component of the original image obtained by using Retinex model [39]; (d) an exampling trajectory of the 3-DOF motions with $A_1 = A_2 = 100$ *pixel*, $A_3 = 12$ *degree* and $Nop = 200$; (e) the corresponding trajectories of each component.
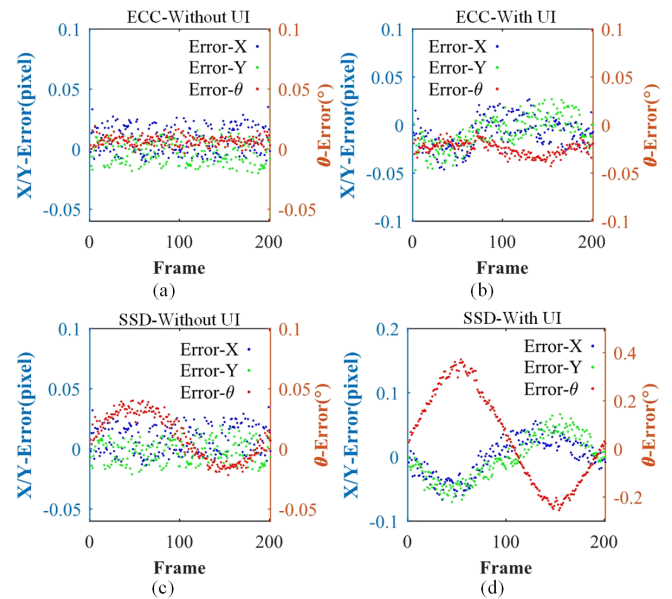

Fig. 3.   Simulations results of the proposed method (ECC) and the method presented in Ref. [34] (SSD) for 3-DOF motion tracking under uneven illumination (UI). (a) and (b) show the measurement errors of the ECC for tracking without UI and with UI, respectively; (c) and (d) demonstrate the corresponding results of SSD.

groups, the performance of the proposed method under two different disturbances (uneven illumination and image noise, respectively) was tested. More specifically, in the first group, two sets of image sequences are generated and used, one of which simulates the uneven illumination and the other does not. In the second group, three sets of image sequences with different noise variances (zero-mean Gaussian noise) are generated and utilized. After obtaining the image sequence, the proposed method and the method presented in Ref. [34] are both implemented for 3-DOF pose tracking. The deviations between the tracked results and the pre-defined poses are recorded and called the measurement errors. In the third group, the time cost of the proposed 3-DOF tracking algorithm is tested and the method shown in Ref. [34] is also implemented for comparison. Note that the template used in the simulation is obtained by cropping from the center area of the image shown in Fig. 2(b), and its resolution is 121×121. For the implemented two tracking algorithms, the maximum number of iterations in each frame is set to 15.

2) Simulation Results: The results of the first simulation group are demonstrated in Fig. 3. As can be seen from the first row of Fig. 3, although measurement errors corresponding to ECC are slightly increased when uneven illumination is involved in the image sequence, they are still distributed over small ranges, i.e., the maximum errors of translation and rotation components are less than ± 0.05 pixel and ± 0.05 degree, respectively. From the second row of Fig. 3, one can see that after adding uneven illumination, the meaasurement errors are apparently increased when use SSD as the

correlation coefficient, i.e., the maximum errors of translation and rotation components reach to ± 0.07 pixel and ± 0.35 degree, respectively. In addition, one can find that the error curves in Fig. 3(d) show the trends of trigonometric functions. The likely reason is that there may be several local optimizations near the real solution of each frame. When uneven illumination is added, it causes the SSD-based tracking algorithm to converge to a local minimum, while the periodic input motion further leads the corresponding measurement errors to show the triangular trends. Comparing the results of ECC and SSD, it can be concluded that the ECC-based 3-DOF tracking algorithm exhibits better performance, especially for the rotation component, when there is uneven illumination during tracking.

Fig. 4 illustrates the results of the proposed method (ECC) and the SSD-based method for 3-DOF motion tracking under different variances of image noise (zero-mean Gaussian noise). One can see that for the measurement of the translation components, both ECC and SSD show high robustness to image noise, i.e., the maximum errors (the height of the dashed line) are smaller than ± 0.05 pixel, and the main errors (the height of the box) distribute at the ranges of ± 0.02 pixel. However, when it comes to the rotation component, the ECC-based tracking method shows higher performance than the SSD-based method. As can be seen from Fig. 4, even through there are outliers, the box height and the maximum errors of the rotation component of the ECC-related results are all lower than the SSD-related results.

Table I shows the time cost of the proposed method and the method present in Ref. [34]. one can see that both the pre-computation time (t_{pre}) and averaged iterative time (t_{it}) of the proposed method are heavier than the method in Ref. [34],
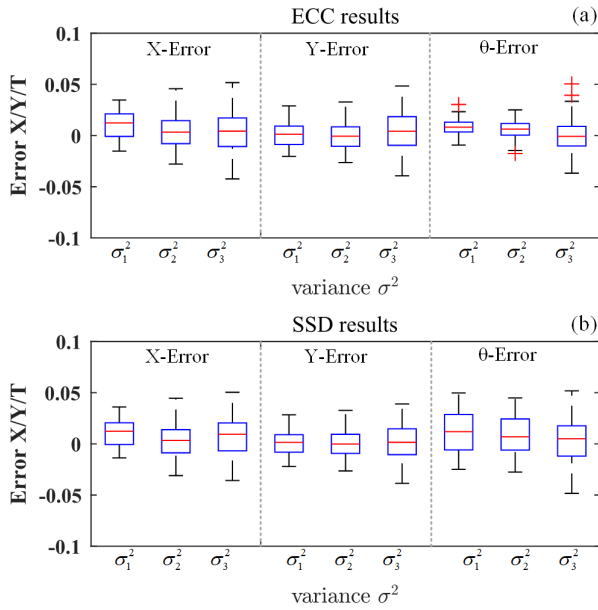
Fig. 4. Simulations results of the ECC and SSD for 3-DOF motion tracking under different image noise variances ($\sigma_1^2 = 0.001$, $\sigma_1^2 = 0.002, \sigma_1^2 = 0.005$). (a) and (b) show the measurement errors of ECC and SSD in Boxplot representation, respectively. Note that the box height represent main error distributions; the red line in the box represents the mean of errors; the two ends of the dashed line represent the maximum and minimum value; the sign of '+' represents the outliers.

TABLE I
THE RESULTS OF TIME COST (NOTE THAT THE ALGORITHMS ARE IMPLEMENTED ON A PC WITH CORE-I7 PROCESSOR PROGRAMMED WITH MATLAB)

Time cost	pre-computation (t_{pre})	per-iteration (t_{it})	per-frame (t_{pf})	Unit
Proposed	9.9	3.6	$K^a * t_{it}$	ms
Ref. [34]	7.5	3.3	$t_{pre} + K^a * t_{it}$	ms

^{a} The maximum iteration number

especially for t_{pre}. This is reasonable, because the complexity of the ECC criterion is obviously higher than that of SSD, and the calculation amount of the algorithms is mainly reflected in the calculation of Hessian and Jacobian matrices. However, for the proposed method, since the Jacobian and Hessian matrices are calculated in the initialization step and there is no need to recalculate in the tracking period, the calculation method of the time cost per-frame ($t_p f$) is thus different from that in Ref. [34] (as shown in the fourth column of Table I). It can be seen that when the maximum iteration number K is smaller than 25, the time cost t_{pf} of the proposed method is smaller than the method in Ref. [34], i.e., the attainable tracking frame rate of the proposed method is higher.

B. Experimental Tests

1) Experimental Setup: To evaluate the practical performance of the proposed method, an experimental system which mainly consists of an optical microscope, a digital camera, a 3-DOF nanopositioner, and a three-CDS based pose measurement system is established, as shown in Fig. 5. Details on the main setups used in the experiments are listed in Table II.
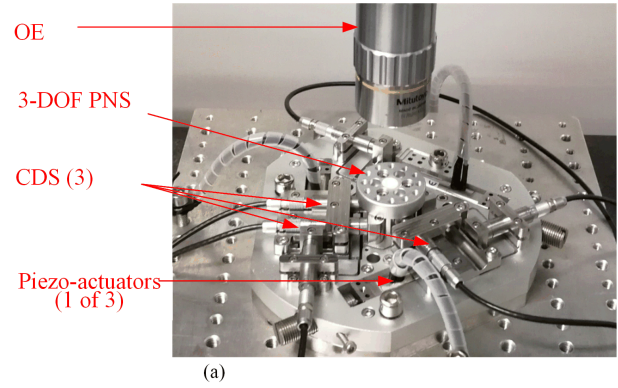

Fig. 5. The experimental system for performance evaluation of the proposed method (OE is the abbreviation of optical microscope).

TABLE II
MAIN SETUPS AND THEIR KEY PARAMETERS USED IN THE EXPERIMENT

Names	Manufacturers&type	Key parameters$_T$
Camera	Tendency Dalsa: Genie TS M2048	Full Resolution: 2048×2048
Microscope	Navitar: 12X UltraZoom; Mitutoyo Objective	zoom ratio: $0.7 \sim 3.55$ $10\times$
Nanopositioner	Self-developed	Working space: $30~\mu m \times 30~\mu m \times 0.24°$
CDS	Physik Instrument: D-E20.200	Resolution: 0.2 nm; Meas. Range: $0 \sim 200~\mu m$

Noth that the control of the self-developed 3-DOF compliant nanopositioner is realized by using the DS1104 R&D controller board from dSPACE GmbH and the visual tracking algorithm runs on a computer with Core i-7 (3.2 GHz) processor programmed with C++.

2) Circular Trajectory Tracking: To verify the performance of the proposed method, we first perform the circular trajectory tracking experiment. Specifically, two circular trajectories with the nominal radii of 8 μm and 12 μm are executed on the nanopositioner, respectively. In addition, in the experiment, the rotation component of the trajectories is set to zero and the frequencies of the vision system and CDS are set to 100 hertz and 1024 hertz, respectively. The measurement results are demonstrated in Fig. 6. It is worth to mention that in Fig. 6 (b) and (c), in addition to the measured results of vision and CDS, two fitting circles obtained based on the CDS data are also presented.

In Fig. 6(a) and (b), one can see that the measured trajectory results of the vision system and the CDS are highly coincident with each other, especially the circular portion, which effectively verifies the effectiveness of the proposed method for pose tracking of the nanopositioner. However, if we look closely at the straight line portion of the trajectory shown in Figs. 6(b) and (c), it can be seen that there is a small angle between the vision results and CDS results. The reason is that in the experiment, the coordinate axes of the nanopositioner and the image sensor are not completely parallel to each other, i.e., there is an initial small rotation angle between them. Moreover, in Fig. 6 (c), one can see that although the fitting circles are obtained based on the measured CDS data, their
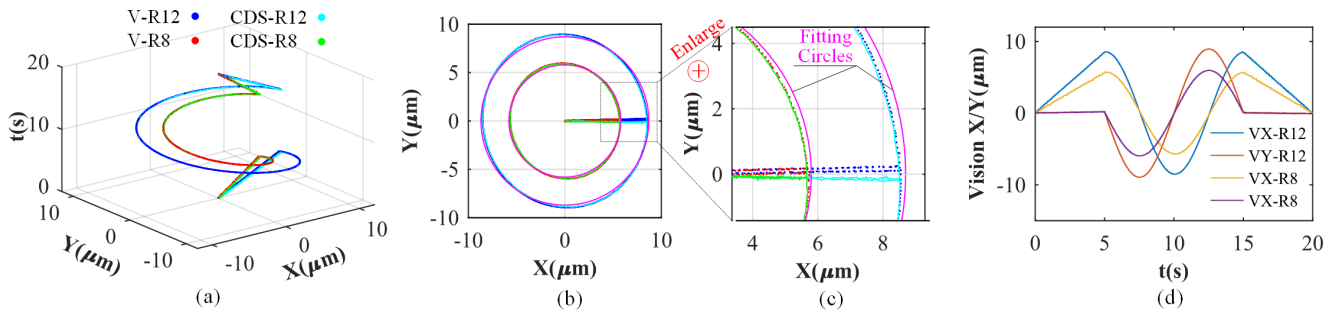
Fig. 6. Tracking results of visual methods and CDS for circular trajectories. (a) Measured results shown in 3-Dimension; (b) trajectories demonstrated in 2-Dimension; (c) partial enlarged figure of (b); (d) tracking results of the vision method shown in each component.

curves are apparently deviating with the measured results. In fact, it can be seen that the measured trajectories are much more like the ellipses. A reasonable explanation is that the input-output model of the compliant nanopositioner used in the experiment is not accurate, so the actual output trajectory is not as expected. Furthermore, in Fig. 6(b) one can see that the measured radii are apparently smaller than the input value. The reason is that due to the existence of hysteresis effect and compliant deformation, the practical output displacement of the piezoelectric actuator is always smaller than the input value.

In order to further investigate the measurement accuracy of the proposed method, it is necessary to evaluate the dynamic tracking errors of the vision method. However, because the visual system and CDS have different acquisition frequencies and they cannot be triggered simultaneously (subject to hardware limitations), their measurement results cannot be directly compared. Besides, there is coupling between the x and y results of the vision method compared to the CDS due to the small rotation angle between their measurement coordinates. To solve this problem, the following scheme is used. First, measurement results of the vision system and CDS corresponding to the circular portion are extracted. Subsequently, the measured CDS results are equally divided into groups, and the group number is equal to the number of visual sampling points in the corresponding measurement period. Third, search for the measurement point closest to the corresponding visual point in each set of CDS results and save them. Finally, the differences between the closest points and the measured vision results are calculated and called as the dynamic tracking errors, as shown in Fig. 7. In Fig. 7, one can see that even when the radii are different, all the dynamic errors distribute in the ranges of ± 0.2 μm, which verify that the tracking accuracy of the proposed vision method is high.

3) Angular Trajectory Tracking: The second performed experiment is pose tracking of an angular trajectory. Specifically, the trajectory of the rotation component is planned to be a step type and the translation components are set to zero. The step size of the rotation angle starts from 0 to a maximum of $0.24°$, then drops to zero, with a step size of $0.04°$ and dwell time of 3 seconds. The sampling frequency of the vision system and the CDS are set to the same with the last experiment. In addition, it is worth mentioning that in this experiment, to reduce the possible interference from
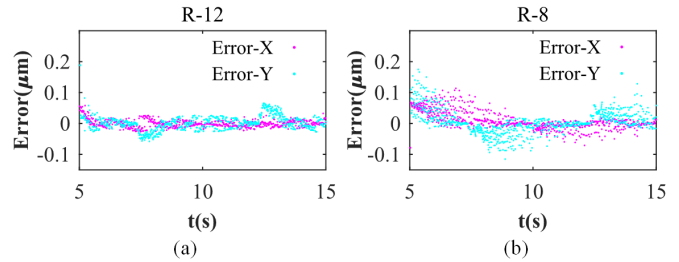

Fig. 7. Dynamic tracking errors of the ECC for circular trajectories. (a) and (b) are the tracking errors of ECC with respect to the radii of 8 μm and 12 μm, respectively.
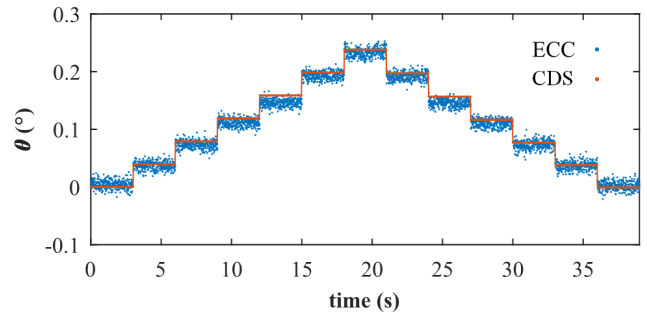

Fig. 8. Tracking results of the ECC and CDS for angular trajectory.

environmental vibration, the focal length of the zoom lens of the vision system is set to the minimum to reduce the system magnification. The measured rotation angle results are shown in Fig. 8. In Fig. 8, it can be seen that although the measurement results of the visual method fluctuate, the overall trend is consistent with the measurement results of the CDS. It is also noteworthy that in this angular tracking experiment, the translation components of the ECC-based vision method are not zero (as shown in Fig. 9) because the rotation center of the nanopositioner is not coincident with the template's center and thus brings parasitic movement.

To quantify the performance of the visual method for angular measurement, we further process the measurement results as follows. First, the measurement results of the CDS and ECC corresponding to each step of the planned trajectory are extracted. Second, the average value corresponding to each step of the two measurement methods are calculated. Third, the measurement results of each step are subtracted from
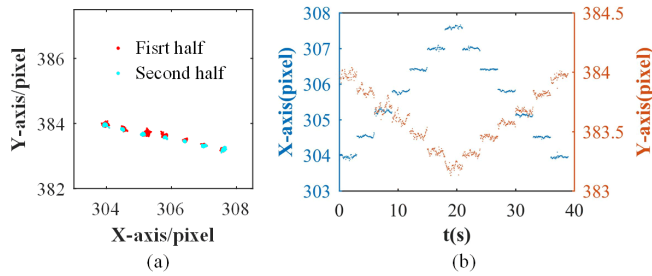
Fig. 9.   Tracking results from the translational components (x,y) of the ECC. (a) Results shown in two-dimensional image space (the first half and second half represent results with respect to the ascent stage and descent stage of the trajectory, respectively); (b) separate results of the translation components shown in one-dimensional.
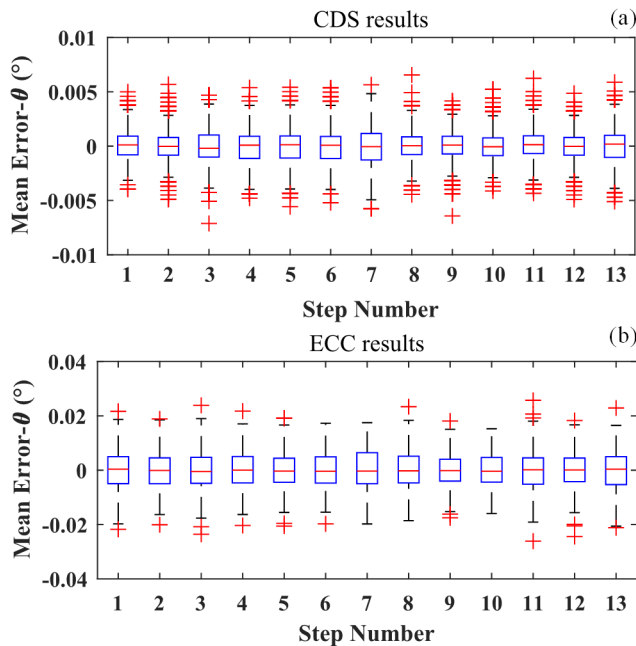

Fig. 10.   The mean errors obtained by subtracting measurement results from the corresponding average value shown in Boxplot representation. (a) and (b) are the results of CDS and ECC, respectively.

the corresponding average value and referred as the mean error. Finally, the average of each step of the ECC results is subtracted from the average of the corresponding CDS results and referred to as the absolute error. It is important to note that herein, the mean error can reveal the repeatability of the evaluated measurement method, and the absolute error reflects the absolute measurement accuracy. Moreover, the SSD-based tracking algorithm is also implemented in this experiment for comparison. Figs. 10 and 11 illustrate the obtained results of mean errors and absolute errors, respectively.

From the mean error results shown in Fig. 10, one can see that the errors of the CDS method are much smaller than the ECC method, i.e., the main errors distribute in the ranges of $\pm 0.002°$ and $\pm 0.005°$, and the extreme errors are about $0.005°$ and $0.02°$, respectively. This is reasonable because as has mentioned in Sec. I, the CDS-scheme uses inverse triangulation to measure the rotation angle, which makes it to benefit a lot from the high resolution of CDS and the large
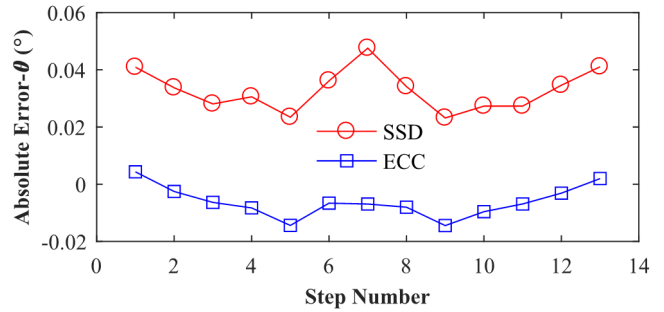

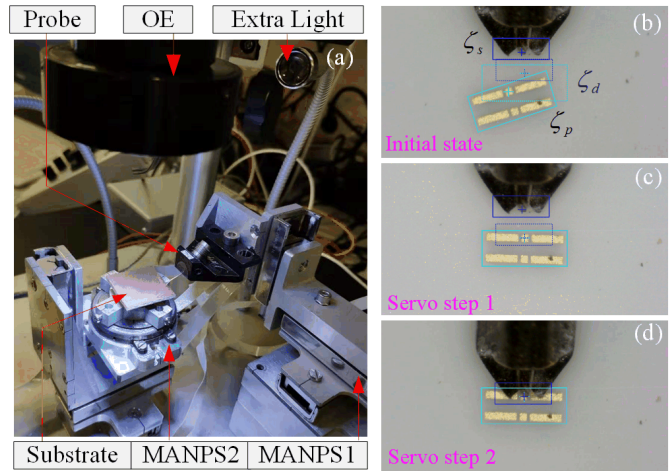Fig. 11.   Absolute measurement error of ECC and SSD for angluar trajectory.

Fig. 12.   The robotic workstation for automatic on-wafer probing. (a) The robotic based workstation which mainly consists of two MANPSs, an optical microscope (OE), a probe and a substrate; (b~d) images corresponding to the three-step process for automatic alignment of the probe and substrate.
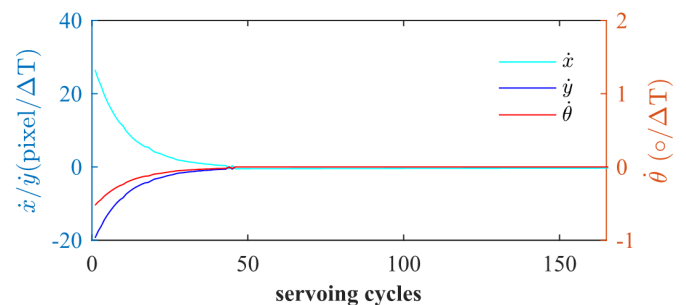
Fig. 13.   Velocity results corresponding to the visual servoing step 1.

distance between two CDS. Nevertheless, it is notable that the performance of the proposed ECC method is very acceptable and commendable, especially when compared with its large measurement range ($0 \sim 360°$). In Fig. 11, one can see that when takes the CDS results as the references, the absolute errors of ECC-based method are apparently smaller than the SSD-based method, which validates that the ECC has better performance than SSD on angular measurement.

C. Discussions

Through the simulations and experiments demonstrated in Sec. IV-A and B, one can see that the proposed method can

effectively track planar 3-DOF motion with high performance. Nevertheless, there are two aspects that need attention in practical applications. First, the measured motion must not contain large fluctuations. In the continuous tracking process, the optimal result of the previous frame is used for the initial guess of the current frame, so large fluctuations may cause the initial guess to be too far away from the optimal solution and thereby resulting in the failure of optimization. Second, although there is no special requirement on the surface of the tracked object (except that the surface should be flat enough to ensure a clear image), the selected template area preferably has a distinct foreground and background, e.g., a stain on the surface of the measured target. If the template contains no texture (constant or near constant) the tracking will failure because the Hessian matrix is (or near) non-positive definite. If similar small features are involved in the template, it may lower the tracking accuracy because there may be several local optimums near the real-solution [23].

V. APPLICATION OF THE PROPOSED METHOD FOR VISUAL SERVOING CONTROL

Since the proposed pose tracking method can effectively measure planar 3-DOF pose without needing artificial markers, it can be easily integrated into a robotic-based micro-/nano-manipulation system for visual servo control of the robot. Herein, according to the practical requirement of automation in RF on-wafer probing described in Ref. [41], a robotic-based work-cell is established and then the probe and substrate are automatically aligned based on visual servo by using the pose information obtained by the proposed method. As shown in Fig. 12(b), the workstation mainly consists of two multi-axis nanopositioning stages (MANPSs) from *Smar Act*, a self-assembled microscope, a substrate, and an infinity probe. Note that the probe and substrate are rigidly connected with MANPS1 and MANPS2, respectively. Moreover, the numbers of DOF of MANPS1 and MANPS2 are three (x,y,z) and four (x,y,z,θ), respectively.

In order to accurately align the tips of the probe to the corresponding locations on the substrate, a three-step strategy is developed, as shown in Fig. 12(b)$\sim$(d). In the first step, the initial poses of the probe ($\zeta_p = (x_{p0}, y_{p0}, 0)^T$) and substrate ($\zeta_s = (x_{s0}, y_{s0}, \theta_{s0})^T$) are detected using two-dimensional template matching and coarse-to-fine three-dimensional template matching [42], respectively. After that, the MANPS2 is controlled to adjust the substrate to the predefined desired pose ($\zeta_d = (x_d, y_d, \theta_d)^T$). Finally, the probe is also moved to the desired pose ζ_d to achieve accurate alignment of the probe and substrate.

Note that, in the last two steps, control of the MANPSs can be realized by using visual servoing. Let **e** be the error between the current pose and desired pose, it can be expressed as

$$\mathbf{e}_*(t) = \zeta_* - \zeta_d \qquad (12)$$

where the subscript $*$ represents the poses of probe or substrate. An exponential decrease ($\dot{\mathbf{e}} = -\lambda\mathbf{e}$) can be used tco minimize the error, and the corresponding control low can be

expressed as [43]

$$\mathbf{v} = -\lambda(\mathbf{L}_e^T\mathbf{L}_e)^{-1}\mathbf{L}_e^T\mathbf{e} \qquad (13)$$

where λ is a proportional gain ($\lambda > 0$), $\mathbf{L}_e$ is the image Jacobian relating the velocities of robot-endeffector and camera.

During the control of MANPS2, the needed 3-DOF pose of the substrate can be obtained by using the method presented in this paper. Since the error function is established in the image space, hand-eye calibration is unnecessary before the experiment, which can greatly simplify the alignment process. Fig. 13 demonstrates the corresponding velocity curves of each axis with respect to the visual servo step 1. The results verify that by using the proposed pose tracking method, accurate and automatic alignment of the probe and substrate can be easily realized.

VI. CONCLUSION

In this paper, an improved template-matching-based pose tracking method for planar 3-DOF nanopositioners is proposed. The more complex but more robust correlation criterion ECC is introduced into the planar 3-DOF motion tracking problem to improve tracking performance. By utilizing the inverse compositional strategy, the corresponding three-parameter nonlinear optimization problem is then efficiently solved. Simulation results show that compared with SSD, the proposed ECC-based method can achieve better tracking performance under the disturbances of image noise and uneven illumination, especially for angular measurement. Besides, the tracking frame rate can be improved even through the matching criterion is more complicated. Experimental results illustrate that compared with the traditional three-CDS measurement scheme, the ECC-based method can not only effectively track pose of the 3-DOF nanopositioner with high accuracy, but the measurement range of rotation angle will not be limited. Finally, the application of automatic alignment of the probe and substrate in on-wafer RF probing verifies the feasibility and practicability of the proposed method.

REFERENCES

[1] C. Shi *et al.*, "Recent advances in nanorobotic manipulation inside scanning electron microscopes," *Microsyst. Nanoeng.*, vol. 2, no. 1, Jun. 2016, Art. no. 16024.

[2] B. Zhu *et al.*, "Design of compliant mechanisms using continuum topology optimization: A review," *Mechanism Mach. Theory*, vol. 143, Jan. 2020, Art. no. 103622.

[3] R. Sakamaki and M. Horibe, "Realization of accurate on-wafer measurement using precision probing technique at millimeter-wave frequency," *IEEE Trans. Instrum. Meas.*, vol. 67, no. 8, pp. 1940–1945, Aug. 2018.

[4] S. Yuan, Z. Wang, N. Xi, Y. Wang, and L. Liu, "AFM tip position control *in situ* for effective nanomanipulation," *IEEE/ASME Trans. Mechatronics*, vol. 23, no. 6, pp. 2825–2836, Dec. 2018.

[5] D. Mukhopadhyay, J. Dong, E. Pengwang, and P. Ferreira, "A SOI-MEMS-based 3-DOF planar parallel-kinematics nanopositioning stage," *Sens. Actuators A, Phys.*, vol. 147, no. 1, pp. 340–351, Sep. 2008.

[6] R. Wang and X. Zhang, "Parameters optimization and experiment of a planar parallel 3-DOF nanopositioning system," *IEEE Trans. Ind. Electron.*, vol. 65, no. 3, pp. 2388–2397, Mar. 2018.

[7] Z. Zhan, X. Zhang, H. Zhang, and G. Chen, "Unified motion reliability analysis and comparison study of planar parallel manipulators with interval joint clearance variables," *Mechanism Mach. Theory*, vol. 138, pp. 58–75, Aug. 2019.

[8] U. Bhagat *et al.*, "Design and analysis of a novel flexure-based 3-DOF mechanism," *Mechanism Mach. Theory*, vol. 74, pp. 173–187, Apr. 2014.

[9] B. Zhu, Q. Chen, H. Li, H. Zhang, and X. Zhang, "Design of planar large-deflection compliant mechanisms with decoupled multi-input-output using topology optimization," *J. Mech. Robot.*, vol. 11, no. 3, Apr. 2019, Art. no. 031015.

[10] W. Gao *et al.*, "Measurement technologies for precision positioning," *CIRP Ann.*, vol. 64, no. 2, pp. 773–796, 2015.

[11] C. Ru *et al.*, *Nanopositioning Technology*. Berlin, Germany: Springer, 2016.

[12] L. Clark, B. Shirinzadeh, Y. Tian, S. Fatikow, and D. Zhang, "Pose estimation and calibration using nonlinear capacitance sensor models for micro/nano positioning," *Sens. Actuators A, Phys.*, vol. 253, pp. 118–130, Jan. 2017.

[13] H. Zang, X. Zhang, B. Zhu, and S. Fatikow, "Recent advances in non-contact force sensors used for micro/nano manipulation," *Sens. Actuators A, Phys.*, vol. 296, pp. 155–177, Sep. 2019.

[14] L. Clark, B. Shirinzadeh, Y. Tian, and D. Oetomo, "Laser-based sensing, measurement, and misalignment control of coupled linear and angular motion for ultrahigh precision movement," *IEEE/ASME Trans. Mechatronics*, vol. 20, no. 1, pp. 84–92, Feb. 2015.

[15] S. Zhao, H. Wei, and Y. Li, "Laser heterodyne interferometer for the simultaneous measurement of displacement and angle using a single reference retroreflector," *Opt. Eng.*, vol. 54, no. 8, Aug. 2015, Art. no. 084112.

[16] S. Pang, X. Zhang, X. Zhang, and Y. Lu, "A magnification-continuous calibration method for SEM-based nanorobotic manipulation systems," *Rev. Sci. Instrum.*, vol. 90, no. 5, May 2019, Art. no. 053706.

[17] B. E. Kratochvil, L. Dong, and B. J. Nelson, "Real-time rigid-body visual tracking in a scanning electron microscope," *Int. J. Robot. Res.*, vol. 28, no. 4, pp. 498–511, Apr. 2009.

[18] L. Clark, B. Shirinzadeh, U. Bhagat, and J. Smith, "A vision-based measurement algorithm for micro/nano manipulation," in *Proc. IEEE/ASME Int. Conf. Adv. Intell. Mechatronics*, Jul. 2013, pp. 100–105.

[19] X. Zhang, X. Zhang, H. Wu, J. Gan, and H. Li, "A high accuracy algorithm of displacement measurement for a micro-positioning stage," *AIP Adv.*, vol. 7, no. 5, May 2017, Art. no. 055301.

[20] C. Zhao, C. Cheung, and M. Liu, "Integrated polar microstructure and template-matching method for optical position measurement," *Opt. Express*, vol. 26, no. 4, p. 4330, Feb. 2018.

[21] F. Zhong, S. He, and B. Li, "Blob analyzation-based template matching algorithm for LED chip localization," *Int. J. Adv. Manuf. Technol.*, vol. 93, nos. 1–4, pp. 55–63, Aug. 2015.

[22] C. Ru, Y. Zhang, H. Huang, and T. Chen, "An improved visual tracking method in scanning electron microscope," *Microsc. Microanal.*, vol. 18, no. 3, pp. 612–620, May 2012.

[23] H. Li, B. Zhu, Z. Chen, and X. Zhang, "Realtime in-plane displacements tracking of the precision positioning stage based on computer microvision," *Mech. Syst. Signal Process.*, vol. 124, pp. 111–123, Jun. 2019.

[24] V. Guelpa, P. Sandoz, M. A. Vergara, C. Clévy, N. Le Fort-Piat, and G. J. Laurent, "2D visual micro-position measurement based on intertwined twin-scale patterns," *Sens. Actuators A, Phys.*, vol. 248, pp. 272–280, Sep. 2016.

[25] Z.-H. Chen and P. S. Huang, "A vision-based method for planar position measurement," *Meas. Sci. Technol.*, vol. 27, no. 12, Nov. 2016, Art. no. 125018.

[26] G. Su, G. Lu, and P. Yan, "Planar motion measurement of a compliant micro stage: An enhanced microscopic vision approach," *IEEE Trans. Instrum. Meas.*, to be published.

[27] B. Pan, "Digital image correlation for surface deformation measurement: Historical developments, recent advances and future goals," *Meas. Sci. Technol.*, vol. 29, no. 8, Jun. 2018, Art. no. 082001.

[28] B. Pan, K. Li, and W. Tong, "Fast, robust and accurate digital image correlation calculation without redundant computations," *Experim. Mech.*, vol. 53, no. 7, pp. 1277–1289, Feb. 2013.

[29] F. Zhong, R. Kumar, and C. Quan, "A cost-effective single-shot structured light system for 3D shape measurement," *IEEE Sensors J.*, vol. 19, no. 17, pp. 7335–7346, Sep. 2019.

[30] T. Wang and Q. Kemao, "Parallel computing in experimental mechanics and optical measurement: A review (II)," *Opt. Lasers Eng.*, vol. 104, pp. 181–191, May 2018.

[31] R. Wu, H. Qian, and D. Zhang, "Robust full-field measurement considering rotation using digital image correlation," *Meas. Sci. Technol.*, vol. 27, no. 10, Aug. 2016, Art. no. 105002.

[32] F. Zhong and C. Quan, "Digital image correlation in polar coordinate robust to a large rotation," *Opt. Lasers Eng.*, vol. 98, pp. 153–158, Nov. 2017.

[33] Z. Jiang, Q. Kemao, H. Miao, J. Yang, and L. Tang, "Path-independent digital image correlation with high accuracy, speed and robustness," *Opt. Lasers Eng.*, vol. 65, pp. 93–102, Feb. 2015.

[34] H. Li, X. Zhang, B. Zhu, and S. Fatikow, "Online precise motion measurement of 3-DOF nanopositioners based on image correlation," *IEEE Trans. Instrum. Meas.*, vol. 68, no. 3, pp. 782–790, Mar. 2019.

[35] H. Li, X. Zhang, H. Wu, and J. Gan, "Line-based calibration of a micro-vision motion measurement system," *Opt. Lasers Eng.*, vol. 93, pp. 40–46, Jun. 2017.

[36] G. D. Evangelidis and E. Z. Psarakis, "Parametric image alignment using enhanced correlation coefficient maximization," *IEEE Trans. Pattern Anal. Mach. Intell.*, vol. 30, no. 10, pp. 1858–1865, Oct. 2008.

[37] S. Baker and I. Matthews, "Lucas-kanade 20 years on: A unifying framework," *Int. J. Comput. Vis.*, vol. 56, no. 3, pp. 221–255, Feb. 2004.

[38] J. Nocedal and S. J. Wright, *Numerical Optimization*. Berlin, Germany: Springer, 2006.

[39] J. McCann, *Retinex Theory*. New York, NY, USA: Springer, 2016, pp. 1118–1125.

[40] H. Li, X. Zhang, Y. Huang, and Y. Shan, "Centerline extraction of stripe imaged by optical microscope," *Opt. Precis. Eng.*, vol. 25, no. 5, pp. 1340–1347, 2017.

[41] F. T. V. Kleist-Retzow, T. Tiemerding, P. Elfert, and O. C. Haenssler, "Automated calibration of RF on-wafer probing and evaluation of probe misalignment effects using a desktop micro-factory," *J. Comput. Commun.*, vol. 4, no. 3, pp. 61–67, 2016.

[42] H. Li, X. Zhang, B. Zhu, Y. Lu, and H. Wu, "Micro-motion detection of the 3-DOF precision positioning stage based on iterative optimized template matching," *Appl. Opt.*, vol. 56, no. 34, p. 9435, Nov. 2017.

[43] F. Chaumette and S. Hutchinson, "Visual servo control. I. Basic approaches," *IEEE Robot. Autom. Mag.*, vol. 13, no. 4, pp. 82–90, Dec. 2006.

Hai Li received the Ph.D. degree in mechanical engineering from the South China University of Technology (SCUT) in 2018. He spent one year as a Postdoctoral Fellow with the Division for Microrobotics and Control Engineering (AMiR), University of Oldenburg, Germany. He is a Postdoctoral Researcher with SCUT. His research interests include vision-based precision measurement and servo control, and micro-/nano positioning, and manipulation.

Xianmin Zhang was born in 1964. He received the Ph.D. degree from the Beijing University of Aeronautics and Astronautics, Beijing, China, in 1993. He has been the Director of the Guangdong Key Laboratory of Precision Equipment and Manufacturing Technology since 2010 and the Dean and the Chair Professor of the School of Mechanical and Automotive Engineering, SCUT, since 2013. His research interests include robotics, precision instrument analysis and design, dynamics, and vibration control of mechanisms.

Sheng Yao received the B.Eng. degree in mechatronics engineering from SCUT, Guangzhou, China, in 2016, where he is currently pursuing the Ph.D. degree with the Guangdong Key Laboratory of Precision Equipment and Manufacturing Technology. His research interests include high-precision vision systems and vision-based control for micromanipulation, with the applications to MEMS and biological cells.

Benliang Zhu received the Ph.D. degree of mechanical engineering from SCUT in 2014. He is currently an Associate Professor with the School of Mechanical and Automotive Engineering, SCUT, and a Guest Scholar with the Graduate School of Engineering, Kyoto University, supported by the JSPS International Fellowship. His research mainly focuses on compliant mechanisms/tools and their applications in the micro/nano-manipulation systems, and other emerging fields.

Sergej Fatikow received the Ph.D. degree in electrical engineering and computer science from Ufa State Aviation Technical University, Russia, in 1988. Since 2001, he has been a Full Professor with the Department of Computing Science and the Head of the AMiR, University of Oldenburg, Germany. His research interests include micro- and nano-robotics automation at nanoscale, nanohandling inside SEM, AFM-based nanohandling, sensor feedback at nanoscale, and neurofuzzy robot control.